Study of the dissociation reaction $n + p \rightarrow p\pi^- + p$ for incident neutron momenta between 50 and 300 GeV/c

J. Biel,* T. Ferbel, P. Slattery, and D. Underwood[†]

University of Rochester, Rochester, New York 14627

B. Gobbi, L. Kenah,[‡] R. Ruchti,** and J. Rosen

Northwestern University, Evanston, Illinois 60201

E. Bleser[††]

Fermi National Accelerator Laboratory, Batavia, Illinois 60510

D. Freytag

Stanford Linear Accelerator Center, Stanford, California 94305

(Received 4 April 1978)

We present results of our study of the neutron dissociation reaction $n + p \rightarrow (p\pi^-) + p$ for incident neutron momenta between 50 and 300 GeV/c. The integrated dissociation cross section for small values of $(p\pi^-)$ mass is essentially constant over this momentum interval. A strong correlation exists between the square of the four-momentum transfer (t) and the $(p\pi^-)$ rest mass, as well as between t and the decay angles of the $(p\pi^-)$ system. The observed $(p\pi^-)$ mass distribution is comprised of contributions from both narrow resonance like peaks and a broad low-mass continuum. Moments of the $(p\pi^-)$ decay angular distributions reveal rich structure, suggesting the presence of many partial waves.

I. INTRODUCTION

Diffraction dissociation of hadrons has been a subject of extensive theoretical and experimental investigation.[1] The intuitive approach of Good and Walker,[2] in particular, has stimulated much research in the area of inelastic fragmentation of hadrons. These kind of processes can be categorized either into inclusive diffraction channels,[3] wherein the cross section is defined as a sum over all possible diffractive final states available to one of the hadrons initiating the reaction, or into exclusive channels,[4] which involve the diffractive fragmentation of hadrons into specific low-multiplicity final states. In this paper we present the results of a study of the neutron-dissociation reaction

$$n + p \rightarrow (p\pi^-) + p \qquad (1)$$

for incident neutron momenta between 50 and 300 GeV/c. Preliminary results from our experiment and comparisons with models have appeared previously in the literature[5]; here we will provide the findings of our completed investigation. Details of the experimental apparatus and of the procedures used in the data analysis are given in Secs. II and III, respectively. In Sec. IV we discuss the extraction of absolute cross sections, and in Sec. V we provide a comprehensive description of the differential spectra measured in this experiment. A summary of the conclusions is presented in the last part of this paper.

II. EXPERIMENTAL DETAILS

The experiment was performed in the M3 beam line of the Fermilab Meson Detector Building. Neutrons were produced through the interaction of 300-GeV/c primary protons in a 20-cm Be target. Secondary particles produced at approximately 1 mrad were selected using collimators located ~10 m downstream of the target. The charged component of the beam was removed using a series of quadrupole and dipole magnets, while three radiation lengths of lead were used to convert photons in the beam into e^+e^- pairs. These were subsequently deflected into collimators by a dipole magnet which was located further downstream. The final beam aperture was defined by a collimator placed at a distance of 200 m from the production target. This collimator was equipped with a variable-aperture insert which allowed adjustment of both size and intensity of the neutron beam. A final series of magnets removed any residual charged particles originating either at the production target or from material along the path of the beam. At the position of our spectrometer (approximately 450 m from the production target) the beam had a radius of about 5 mm and was essentially free of halo. For momenta in excess of 50 GeV/c, the beam was composed mainly of neutrons with minor ($\lesssim 1\%$) γ, K_L^0, and $\bar{n}$ contamination.[6]

Beam particles interacted with target protons contained in a high-pressure hydrogen-gas target.

Gas was chosen in place of liquid hydrogen in order to be able to detect recoil protons with very small momenta. The target consisted of a cylindrical region, 9 cm in diameter and 50 cm long, enclosed within a pressure vessel and surrounded by a scintillation-counter system. Two thin disc-shaped counters, A_0 and S, were placed at the extreme ends of the target region. A_0 was used to veto events which were initiated by charged incoming particles, and S was used to trigger on forward-going reaction products. The remaining, azimuthally located, 16 counters (Fig. 1) were $\frac{1}{4}$-in. thick scintillators used to detect the recoiling protons. Pressures of up to 3000 psi could be maintained within the target. (At this pressure, hydrogen gas has approximately 20% of the density of liquid hydrogen.) Light produced within the scintillators was transferred via Lucite light pipes and windows into phototubes positioned outside the pressure vessel. To insure reliable operation, counters A_0 and S were monitored using two phototubes for each counter. The recoil counters were paired at each end and each pair was viewed with an individual phototube. Counter pairs were staggered at the opposite ends of the target to provide definitive identification of the activated scintillator strip.[7] Three kinds of information were sought from the recoil counters: (1) The azimuthal direction of the recoil proton; (2) The position along the length of the target where the proton had struck the scintillator (determined from the ratio of the relative pulse heights at the two ends of the scintillator); (3) The energy deposited in the scintillator strip (determined from the combined pulse heights at the two ends of the scintillator strip).

The dissociation products of the neutron were detected using a standard spark-chamber spectrometer (Fig. 2). Principal components of this system were: (1) a trigger-counter system, (2) 30 planes of wire spark chambers, (3) a momentum-analyzing magnet, and (4) a small beam calorimeter.
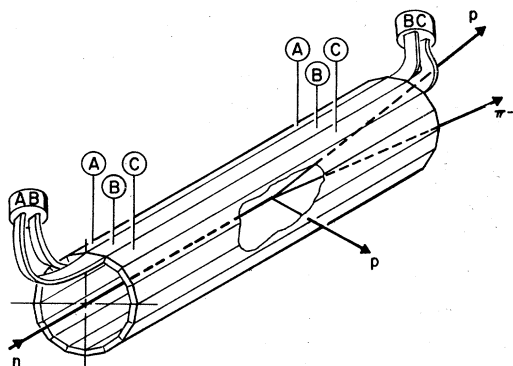
The scintillation counters were used to establish conditions for an acceptable dissociation event. One array of veto counters, A_1-A_4, which covered the front face of the spectrometer magnet was used to signal the presence of any particles which might have missed the magnet aperture. These counters were positioned behind a 2-cm sheet of lead to enhance the detection of photons. Downstream of the magnet, particles passed through a six-element counter hodoscope (H1). Finally, a second hodoscope of 16 counters (H2) was located at the extreme downstream end of the spectrometer.

The spark chambers were used to determine the trajectories of charged particles within the spectrometer. The spark positions were determined using a magnetostrictive-read-out technique which provided a positional accuracy of approximately ±0.3 mm. To provide the system with a degree of redundancy, the signals were recorded from both ends of each magnetostrictive readout line.

Momentum analysis of charged particles was achieved using a BM109 dipole magnet with an aperture of 20 cm (height) by 60 cm (width). An 18-kG field extending 1.9 m along the z direction delivered a transverse-momentum impulse of approximately 1 GeV/c in the horizontal direction. Particle momenta were determined to better than 1% accuracy.

A small hadron calorimeter was located downstream of the spark chambers, approximately 26 meters from the hydrogen target. The calorimeter was constructed of 21 iron plates, 10 cm × 10 cm × 2.5 cm in size, interleaved with 10 cm × 10 cm × 0.6 cm sheets of plastic scintillator; the total corresponded to approximately three absorption lengths of material. Discriminator levels on the photomultiplier tubes viewing the sheets of scin-

FIG. 1. Illustration of the scintillator arrangement inside the gas target.
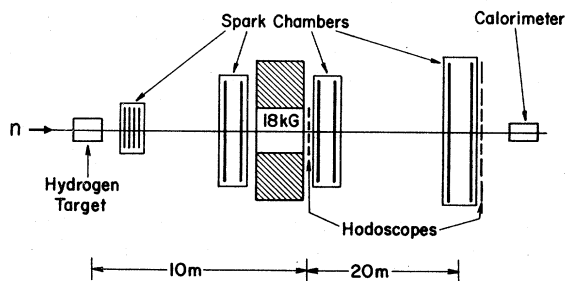

FIG. 2. Neutron-dissociation spectrometer.

tillator were set low enough to detect any charged particles incident upon or produced within the calorimeter. One of the reasons for augmenting the spectrometer with this device was to detect background multibody dissociation processes such as

$$n + p \rightarrow n + \pi^+ + \pi^- + p \, . \tag{2}$$

These kind of reactions are characterized by high-energy neutrons produced in the forward direction. The calorimeter was also used to count the number of neutrons in the beam, and thereby provide a normalization for our measurements of the dissociation cross section.

Trigger requirements for the experiment were established using coincident signals from the scintillation-counter system. A candidate event was required to have: (1) At least one charged-particle present immediately downstream of the target region, (2) At least two particles traversing the H1 hodoscope, (3) A recoil proton detected within the hydrogen target, (4) No signal in any of the spectrometer veto counters. The trigger rate was an approximately linear function of target pressure with about one trigger per 10^7 incident neutrons per psi of hydrogen within the target. The first 25% of the data was taken with a target pressure of 1250 psi, but for the remainder of the experiment the pressure was reduced to 750 psi, allowing lower-energy recoil protons to reach the recoil counters. At the lower pressure there were 5–10 triggers per machine cycle (a five second acceleration cycle followed by a one second spill) for about 2×10^5 incident neutrons per spill. The results presented in this report represent the analysis of approximately 4×10^5 triggers. The data were collected in two roughly equal running periods.

III. ANALYSIS OF DATA

The reconstruction process commenced with the examination of signals from counters located within the hydrogen target. All pulse heights from the azimuthal recoil counters were checked to assure that the two largest signals were from phototubes located at opposite ends of the same recoil scintillator. Events for which this was not the case lacked a unique signal for the recoil proton and were therefore removed from further consideration. Approximately 85% of all triggers passed this requirement. In subsequent discussion, the phototube signals from the recoil counters will be referred to as A_{up}, for the upstream end of the target, and A_{down} for the downstream end of the target.

Using the spatial coordinates of sparks detected in the spark chambers, a search was performed

for particle tracks within the spectrometer. After all possible track candidates were located, tentative Vee candidates were formed by pairing each positive track with each negative track. Events for which no pair of oppositely charged tracks could be found were discarded.

The reconstructed longitudinal coordinate of each Vee candidate was often uncertain to several tens of centimeters; this was because of the small opening angle between the two tracks of the Vee upstream of the magnet. This uncertainty in the z position was greatly reduced by using the recoil scintillators to determine the location of the interaction vertex. Assuming an exponential loss for light travelling along these scintillator strips, we can express the observed pulse height at either end of the strip as follows:

$$A_{up} = \epsilon_{up} A e^{-az} , \tag{3}$$

$$A_{down} = \epsilon_{down} A e^{-a(l-z)} , \tag{4}$$

where A is proportional to the ionization produced by the recoil proton within the scintillator, z is the position along the scintillator at which the recoil entered the strip, a is the attenuation coefficient for light travelling through the scintillator, and ϵ_{up} (ϵ_{down}) is the efficiency of the upstream (downstream) light guide and phototube system. Solving for z, we have

$$z = C_1 \ln \frac{A_{down}}{A_{up}} + C_2 , \tag{5}$$

where the constants C_1 and C_2 are determined for each scintillator by reconstructing a small fraction of the data (without using information from the hy-
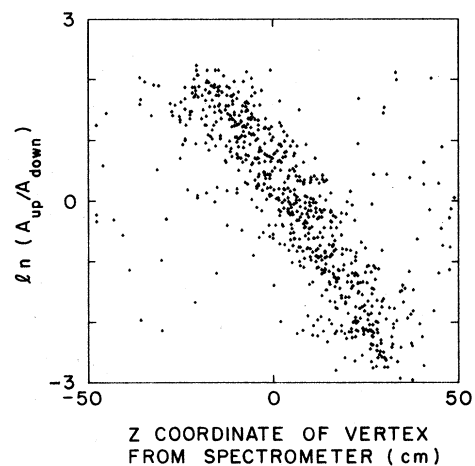

FIG. 3. Scatter plot of the logarithm of the ratio of the pulse heights observed at opposite ends of the recoil scintillators versus the z coordinate of the dissociation event as determined by the tracks obtained using the spark chambers.

drogen target) and plotting the reconstructed z co-ordinate of the vertex as a function of $\ln(A_{\text{down}}/A_{\text{up}})$. Figure 3 illustrates the correlation observed for a typical target counter. (For this plot we used only events with large opening angles and, therefore, small errors in the z coordinate of the vertex.)

Upon locating the track elements and the inter-action vertex [using expression (5)], an iterative least-squares fit was performed to the spark posi-tions. Those sparks which deviated by more than 2 mm from a fitted trajectory were removed. If in the initial fit the same spark was used for both tracks of the $(p\pi^-)$ "vee", then subsequent to the first iteration, that spark was assigned to the best matching trajectory. After the fit, those track pairs with a high χ^2, or with a track containing too few sparks, were dropped from further considera-tion. Events which had more than two tracks were then subjected to more detailed examination. Many of these events contained sets of tracks which were

nearly identical in their spark composition. In such cases, only the highest-quality track (deter-mined by the relative χ^2 and the number of sparks) was retained. If, after this selection, more than a single vee still remained, the event was then re-jected. Approximately 60% of all triggers sur-vived the entire reconstruction process.

Next, using a Monte Carlo technique, the data were corrected for various geometric cuts and losses. By generating an ensemble of fictitious events with the same kinematic properties as the real data but with random values for the interac-tion vertex (X_v, Y_v, Z_v) and for the azimuthal angle of the recoil proton (using ranges for these quanti-ties as observed in the data), a weight was ob-tained for each observed event. Each member of the generated ensemble was then tested to see whether it would have satisfied the trigger re-quirements of our spectrometer. The event weight (W) was then taken to be as follows:

$$W = \frac{\text{number of generated events in the ensemble}}{\text{number of ensemble events that would have produced triggers}}. \tag{6}$$

Enough Monte Carlo events were generated for any accepted event to assure that the statistical error on the weight was at most 10%.

The experimental events were also tracked through the apparatus, and a few percent of these were found to fail the Monte Carlo acceptance cri-teria; this was presumably due to the idealized ge-ometry in the efficiency calculation. The events which failed this check were eliminated from the sample because they were already compensated for by the events remaining in the sample. Plots of the average geometric efficiency of the spec-trometer as a function of momentum (p), mass (M), and square of the four-momentum transfer from the neutron to the $p\pi^-$ system (t) are pre-sented in Fig. 4.

The geometric acceptance of the spectrometer deteriorates rapidly for neutron momenta below 50 GeV/c. This problem is further aggrevated by the difficulty in reconstructing tracks with mo-menta below 5 GeV/c. Furthermore, as will be shown in the following sections, background cor-rections are most important at low beam momenta. For the above reasons, events with reconstructed neutron momenta below 50 GeV/c were not re-tained for further investigation.

In addition to calculating a weight for each ob-served event, the acceptance of the apparatus was also studied using events generated over all re-gions of phase space. This simulation revealed the existence of a kinematic region for which the geometric acceptance was <1%. The biased re-

gime corresponds to values of $\cos\theta > 0$ (of the pro-ton in the Gottfried-Jackson frame of the $p\pi^-$ sys-tem), and is strongly dependent on mass and inci-dent neutron momentum. For small M values, this bias is limited to very low momenta (<50 GeV/c), but for masses of 2 GeV the problem is
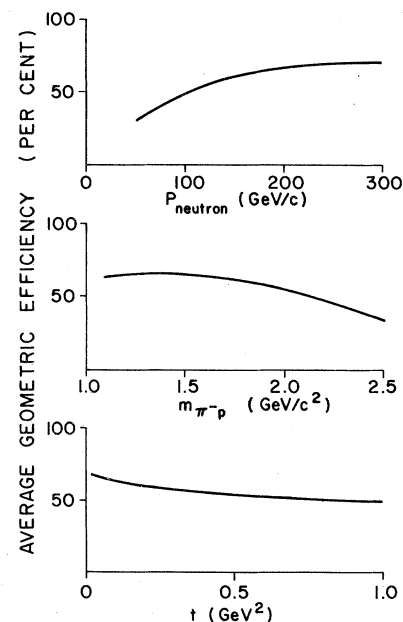

FIG. 4. Plots of the average geometrical efficiency as a function of p, M, and t.

(a)

CALORIMETER PULSE HEIGHT

(b)

PULSE HEIGHT < 25

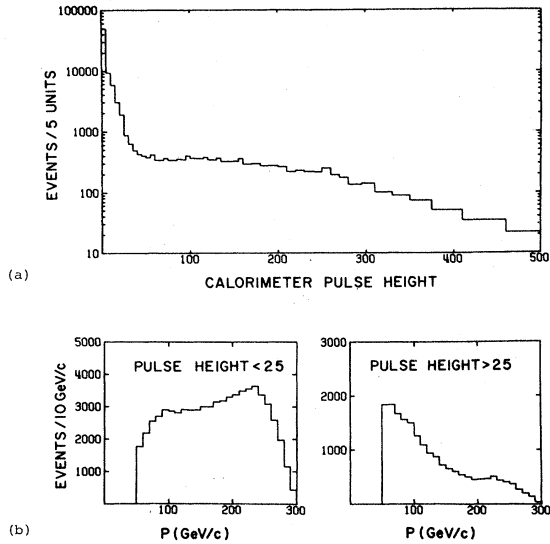PULSE HEIGHT > 25

P (GeV/c)   P (GeV/c)

FIG. 5. (a) A histogram of the calorimeter pulse heights. (b) Histograms of the neutron momenta observed for events with calorimeter pulse heights less than and greater than 25.

significant up to momenta of approximately 200 GeV/c. The Monte Carlo weight calculation described above corrects only for lost events if other similar events are present, and is consequently inadequate for handling a region of miniscule acceptance. Experimental evidence for such gross losses, as well as the steps taken to correct them, will be discussed later in this paper.

As was mentioned in Sec. II, the calorimeter, located downstream of the apparatus, was intended as an aid in suppressing backgrounds such as those provided by reaction (2). In a substantial fraction of events of this type, the final-state neutron will have a momentum and direction similar to that of the incident neutron beam. Figure 5(a) displays the experimentally observed distribution of the sum of pulse heights from the three phototubes of the calorimeter. While the bulk of the data have small pulse heights, a long tail to the distribution, extending to very large pulse heights, is evident. (The small fraction of events for which the trajectory of one of the reconstructed charged-particle tracks of the vee intersected the calorimeter position was removed from the distribution.) The energy deposited in the calorimeter can be attributed to secondary interactions of neutral hadrons in the calorimeter. Events with a pulse height of 25 or greater were judged to result from interactions of secondary neutrons, and these events were consequently eliminated from consideration. An indication that this interpretation was sound was based on the reconstructed momentum

spectrum of incident neutrons for events with calorimeter pulse heights above 25. When compared to the spectrum for events with small pulse heights [Fig. 5(b)], the data with large pulse heights show a rather dramatic low-momentum enhancement. Because the observed charged secondaries in reactions such as reaction (2) carry away only a small fraction of the incident beam momentum, this result confirms essentially what might be expected from such background triggers.

The pulse-height information obtained from the counters surrounding the hydrogen target proved to be surprisingly valuable in eliminating background events. To begin with, the azimuthal angle of the recoil proton, calculated from the π^- and p momenta, was compared with the angle determined from the position of the activated recoil counter. A typical distribution in the difference (ϕ) between the calculated recoil angle of the proton and the angle observed for the recoil, for one of the 16 azimuthal counters, is shown in the lower portions of Fig. 6(a). Most of the events have a ϕ angle within the angular resolution of the recoil counter ($360°/16 = 22.5°$). As in the case of events with large pulse heights in the calorimeter, we attribute events outside of the peak to background reactions involving missing neutrals, e.g., reaction (2) and

$$n + p \rightarrow p + \pi^- + \pi^0 + p \,. \tag{7}$$

For these types of events, the calculation of ϕ is based only upon the observed charged tracks and therefore cannot yield the correct direction of the recoil proton. Again, as in the case of events with large pulse heights in the calorimeter, the possibility of the presence of additional missing neutrals is corroborated by a low-momentum enhancement in the beam spectrum for events outside of the peak region in ϕ.

Background to reaction (1) was further suppressed by examining the energy deposited by the recoil proton in the scintillators surrounding the hydrogen target. Using Eqs. (3) and (4) we can define an average pulse height $\overline{A}$ as follows:

$$\overline{A} = (A_{up} A_{down})^{1/2} = (e^{-al} \epsilon_{up} \epsilon_{down})^{1/2} A$$
$$= CA \,, \tag{8}$$

where C is a constant which depends on the nature of each recoil counter. Because the squared four-momentum transfer t can be written as

$$t = 2m_p T \,, \tag{9}$$

where m_p is the mass of the proton and T is the kinetic energy of the recoil proton in the laboratory, we can conveniently use t as a measure of T. A plot of $\overline{A}$ vs t, for a typical recoil counter,
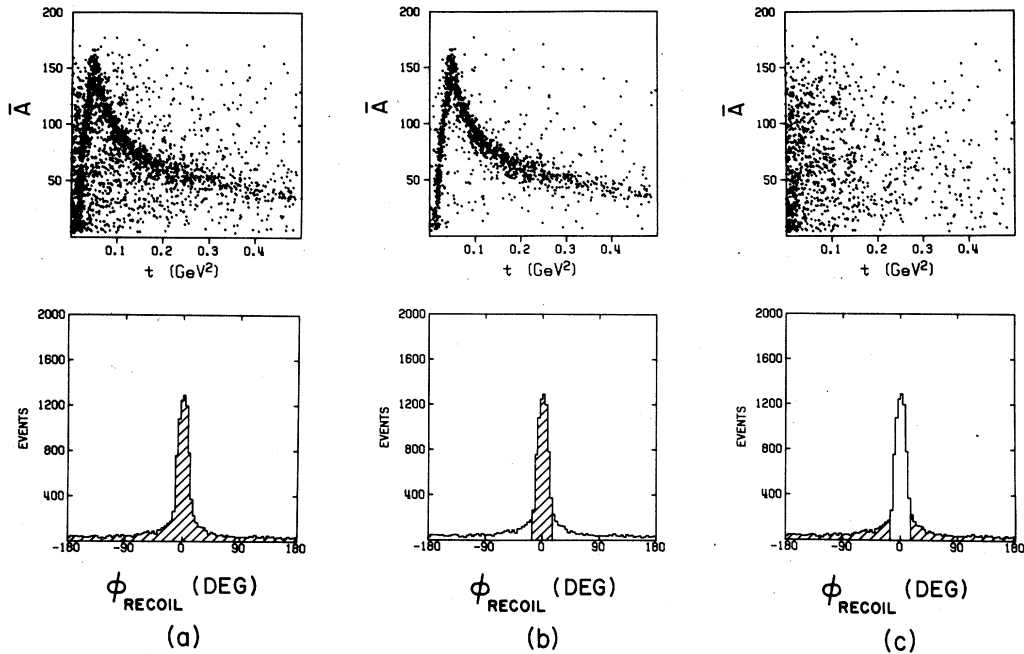
FIG. 6. Mean value of the pulse heights versus t for a typical recoil scintillator for the following three conditions: (a) All events. (b) Events with recoil angles less than 14°. (c) Events with recoil angles greater than 14°.

is given in the upper portion of Fig. 6(a). In this figure, a band of high density is seen to rise linearly from the lower left-hand corner up to a t of approximately 0.06 GeV^2. For larger t, the band decreases in value and appears to approach asymptotically a horizontal line as t increases. The above description is in complete agreement with the expected signal from recoil protons. If the recoil has little kinetic energy, the proton will stop within the scintillator, depositing all its energy and producing a pulse height proportional to T (and therefore to t). As T of the proton increases, the recoil will eventually pass through the scintillator and deposit less than its total kinetic energy. At large values of T, the energy deposited within the scintillator will approach the value expected for a minimum-ionizing particle.

When data are divided into regions of small and large ϕ [Figs. 6(b) and 6(c)], those events with small values of ϕ are found to have a much cleaner energy-loss distribution. Using plots similar to those shown in Fig. 6, events with improper recoil pulse heights were removed. As was the case with other backgrounds, the momentum spectrum for the events removed due to their having improper pulse heights shows the low-momentum enhancement expected from the final state containing missing neutrals. (Events with t values below 0.02 GeV^2 were discarded from the data sample because most of these would have protons with in-

sufficient recoil energy to reach the counters and produce a trigger.)

In addition to removing background by rejecting events with pulse heights outside of the signal band, we also imposed a cutoff on the ϕ recoil angles. An event with a recoil angle whose absolute value was less than 14° was considered as an acceptable candidate for reaction (1). We corrected this "signal" region of the data by subtracting from it events whose recoil angles had magnitudes between 14° and 28° (the "background" region); this had the effect of approximately compensating for background events remaining in the signal region. (An additional refinement was added to this procedure in order to correct for resolution error in our determination of the recoil angle. See Ref. 7.)

During the experiment, runs were taken with all hydrogen gas evacuated from the target. These data could then be subtracted from the normal data to correct for interactions occurring in material other than the high-pressure hydrogen gas. When normalized to the same incident neutron flux, the target-empty correction was found to be less than 0.3%. In addition, because experimental distributions for target-empty and for target-full were very similar, the net effect of this correction was completely negligible. One interesting aspect of the target-empty data is the distribution in the Z_v coordinate (Fig. 7). In contrast to the smooth dis-
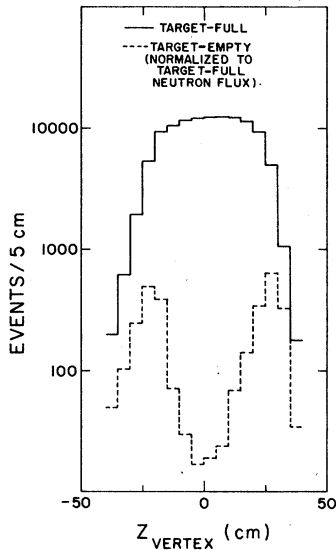
FIG. 7. Vertex distributions for target-full and target-empty runs.

tribution obtained for the target-full data, the target-empty events exhibit two peaks, corresponding to the locations of the veto and the trigger counter within the gas target.

The final data sample consisted of a signal of approximately 60 000 events and a background of approximately 10 000 events. The average weight per event was ~2.0.

IV. CROSS SECTIONS AND NORMALIZATION

Several corrections were included in the calculation of the cross section. The first of these was a $(10 \pm 3)\%$ correction for losses due to reconstruction inefficiency. Second, was a correction of $10 \pm 3\%$, made to account for the fact that events with neutron momenta below 50 GeV/c were not used as data but were counted in the calorimeter. Another 5% correction to the neutron flux was made to account for noninteracting beam neutrons which failed to register in the calorimeter. Two additional important corrections, described below, were then applied to the data.

One of these corrections was required because the experiment contained regions of exceedingly poor geometric efficiency. The events affected by this problem were principally of low momentum, high mass ($M \gtrsim 1.5$ GeV), and $\cos\theta_{GJ} > 0$. (The polar angle θ_{GJ}, as indicated before, is the Gottfried-Jackson angle of the proton in the $p\pi^-$ rest frame.) At small mass values the observed cross section for reaction (1) was found to be nearly energy independent, while at high masses it was found to rise, approximately linearly, with increasing momentum. Because this relatively

strong momentum dependence of the cross section was found only for regions of poor acceptance ($\cos\theta_{GJ} > 0$), we attributed the effect to limitations in our calculation of the efficiency of the apparatus. To correct for such additional losses at high mass, low momentum, and $\cos\theta_{GJ} > 0$, we assumed that the shape of the distribution in θ_{GJ} was energy independent (this was the case for $\cos\theta_{GJ} < 0$). The cross section for all θ_{GJ} as a function of neutron momentum was then written as the product of the measured cross section for $\cos\theta_{GJ} < 0$ (where the acceptance of the spectrometer was good) and a momentum-independent ratio of the cross section for all $\cos\theta_{GJ}$ to the cross section for $\cos\theta_{GJ} < 0$. The latter momentum-independent ratio was determined from data at high momenta, where spectrometer losses were judged to be small.

To correct differential cross sections for the above-described low-momentum losses, the data were treated as follows. For any given ($p\pi^-$) mass we defined a value of momentum, below which the event was rejected [the cutoff value was chosen to be an increasing function of mass $P_c(M)$]. This cut eliminated from the differential spectra those portions of the data containing significant losses in θ_{GJ}. The surviving events were then increased in weight to correct for the loss in cross section caused by the momentum cut. Assuming that the dissociation process is nearly momentum independent, this additional weight was taken to be the inverse of the integrated probability for having an incident neutron with momentum greater than $P_c(M)$. That is, for the neutron beam-momentum probability distribution labeled $f(p)$, the correction to the weight for the event, $W(M)$, is defined as

$$W(M) = 0, \quad \text{for } p < P_c(M)$$

$$W(M) = \left[\int_{P_c(M)}^{300} f(p)dp \right]^{-1}, \quad \text{for } p > P_c(M). \quad (10)$$

A similar procedure, but with a more restrictive cutoff in $P_c(M)$, was used for calculating the sensitive moments of the spherical harmonics for the decay angles of the $p\pi^-$ system (θ_{GJ}, ϕ_{GJ}).[7]

Finally, a correction to the total cross section was applied for events with t values below 0.02 GeV^2. This was done by extrapolating an assumed exponential falloff of the cross section in t from the observed t values to $t = 0$. A more detailed description of the parameters used in these extrapolations will be given later in this paper.

Table I presents a summary of the corrected cross sections obtained in this experiment. The data indicate approximate energy independence of the yield for momenta between 50 and 300 GeV/c.

TABLE I. Final cross sections.

Momentum interval (GeV/c)	Mean momentum (GeV/c)	σ (μb)
50–115	85	273 ± 41
115–160	140	296 ± 40
160–195	180	303 ± 37
195–220	208	299 ± 34
220–250	235	314 ± 33
250–300	265	319 ± 31
50–300	200	301 ± 23

V. EXPERIMENTAL SPECTRA

A. General features

The overall weighted distributions in t, M, $\cos\theta_{GJ}$, ϕ_{GJ}, $\cos\theta_H$, and ϕ_H are displayed in Fig. 8. (The subscript H refers to the helicity frame of the $p\pi^-$ system. That is, the axis of quantization is the line of flight of the $p\pi^-$ system in the overall center of mass of the collision. The azimuthal ϕ_{GJ} is often referred to as the Treiman-Yang angle.) The t distribution is exceedingly steep at small t values, and less so at large t. $d\sigma/dM$ is characterized, primarily, by a broad low-mass enhancement. In addition, there are peaks at

masses of approximately 1.38, 1.48, and 1.65 GeV, followed by a smooth fall-off beyond 1.8 GeV. The distribution in $\cos\theta_{GJ}$ shows a strong forward and a smaller backward peak, while the corresponding $\cos\theta_H$ plot is nearly flat with a pronounced minimum in the forward direction. (The detailed nature of this minimum, however, occurs in the region of worst acceptance and is consequently somewhat sensitive to our weighting procedures.) Both the ϕ_{GJ} and the ϕ_H distributions have maxima at ±180 degrees, and the cross section has a small additional peak at $\phi_H = 0$. Both ϕ distributions are symmetric about the origin, as is required by parity conservation (assuming an unpolarized beam of neutrons). For this reason, all further discussion of these variables can be limited to their absolute values. We will examine these data in greater detail in the following sections of this chapter.

B. Distributions in momentum transfer

1. Mass dependence

Our data show a strong variation of $d\sigma/dt$ with the mass of ($p\pi^-$) system. In Fig. 9, t distributions are presented for eight mass intervals, ranging from threshold to 2 GeV. For the higher-mass regions, $d\sigma/dt$ is, with the exception of a possible turn over at small t, well approximated
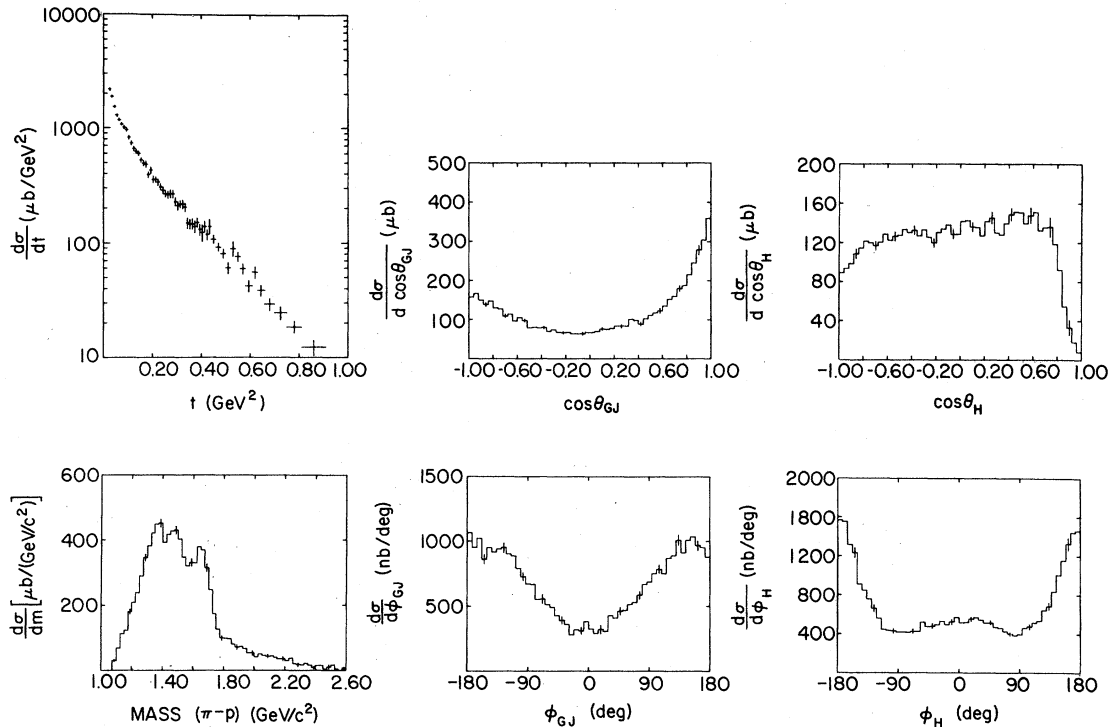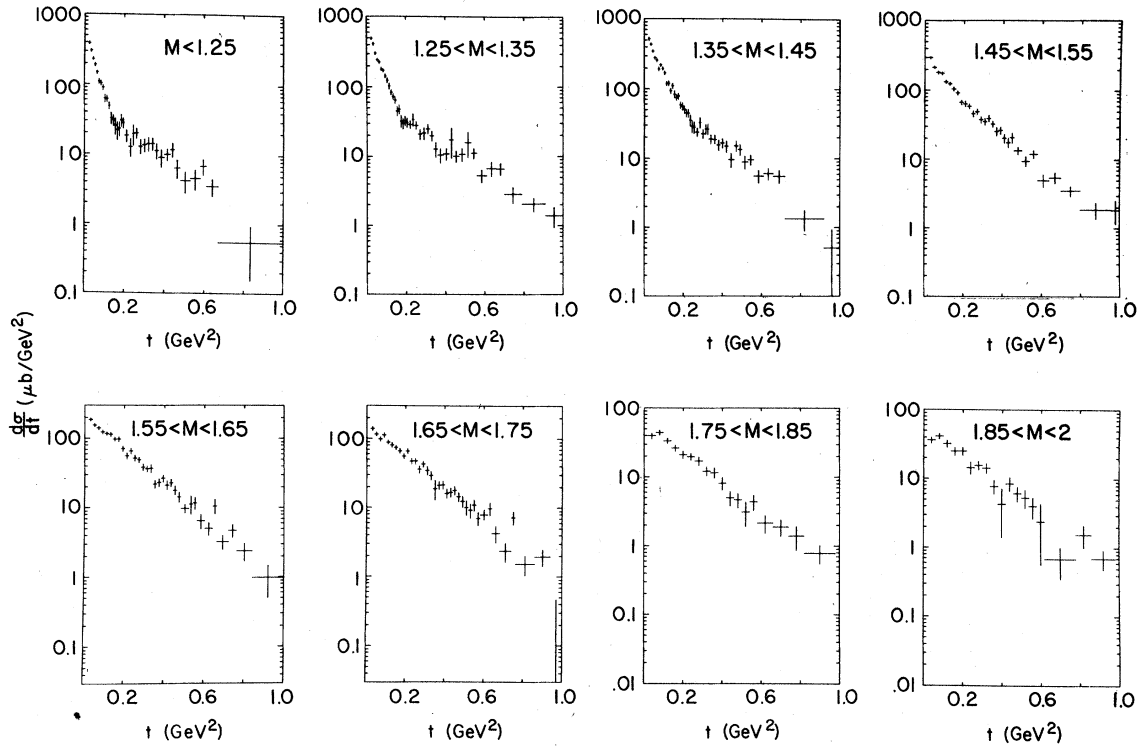

FIG. 8. Histograms showing the final differential cross sections obtained as a function of t, M, $\cos\theta_{GJ}$, ϕ_{GJ}, $\cos\theta_H$ and ϕ_H.

FIG. 9. Distributions in t for eight mass regions.

by a simple exponential. The data below a mass of about 1.5 GeV show more structure. At very small values of t, the cross section is peaked steeply and displays an abrupt change in the shape of $d\sigma/dt$ near 0.2 GeV^2, beyond which the low-mass data appear to fall off in t at a rate comparable to that observed for the data at high mass.

Fits to $d\sigma/dt$ were made using the parametriza-

TABLE II. Fits to differential cross sections [exp($-bt$)].

Mass interval (GeV/c^2)	t range for fit (GeV^2)	b (GeV^{-2})
<1.165	0.03–0.15	24.4 ± 1.6
1.165–1.25	0.03–0.15	19.2 ± 0.9
1.25 –1.3	0.03–0.15	16.8 ± 0.9
1.3 –1.35	0.03–0.15	16.0 ± 0.7
1.35 –1.4	0.03–0.15	15.0 ± 0.65
1.4 –1.45	0.03–0.15	11.2 ± 0.8
1.45 –1.5	0.03–0.19	8.8 ± 0.6
1.5 –1.55	0.03–0.19	6.3 ± 0.6
1.55 –1.6	0.03–0.49	6.1 ± 0.25
1.6 –1.65	0.03–0.49	5.1 ± 0.2
1.65 –1.7	0.03–0.49	5.1 ± 0.2
1.7 –1.75	0.03–0.49	5.1 ± 0.3
1.75 –1.85	0.03–0.44	4.8 ± 0.4
1.85 –2.0	0.03–0.44	4.6 ± 0.4

tion $d\sigma/dt = A \exp(-bt)$. The use of this parametrization is quite common in the study of diffractive reactions, and we will subsequently refer to b as the "slope parameter" of the t distribution. At small mass values, the upper limit of the t interval over which the fit was performed was carefully chosen to include only those values of t that were well approximated by a simple exponential. The results of the fits are listed in Table II, and the values of b are plotted in Fig. 10. Starting with a slope of about 25 GeV^{-2} at small M, a value approximately twice that observed for proton-proton elastic scattering, b drops steadily as the mass increases. Although the dependence on mass is
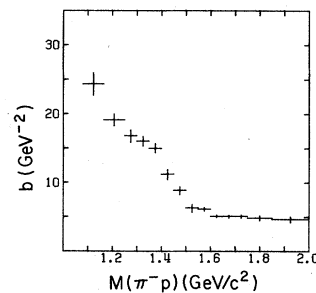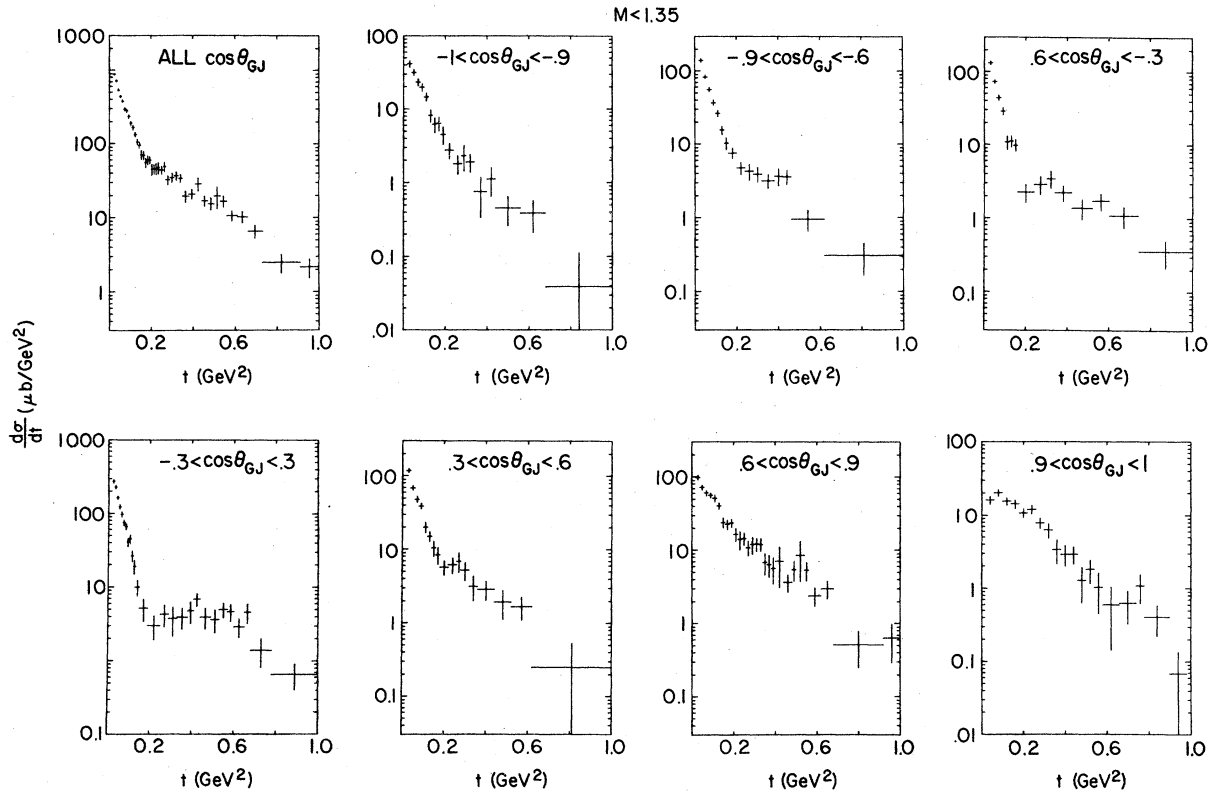

FIG. 10. Slope parameters of t distributions as a function of mass.

TABLE III. Slope parameter as a function of mass and incident momentum.

Mass interval (GeV/c^2)	Momentum interval (GeV/c)	t range for fit (GeV^2)	b (GeV^{-2})
<1.25	50−100	0.03−0.15	18.2 ± 3.9
	100−165		22.5 ± 1.6
	165−205		22.7 ± 1.6
	205−240		19.6 ± 1.4
	240−300		17.5 ± 1.4
1.25−1.35	50−100	0.03−0.15	11.3 ± 2.6
	100−165		15.9 ± 1.3
	165−205		16.4 ± 1.0
	205−240		16.0 ± 1.0
	240−300		16.5 ± 1.0
1.35−1.45	50−100	0.03−0.15	10.2 ± 2.1
	100−165		12.4 ± 1.1
	165−205		13.2 ± 1.0
	205−240		12.8 ± 1.0
	240−300		14.4 ± 1.0
1.45−1.55	50−100	0.03−0.21	5.7 ± 1.7
	100−165		7.0 ± 0.8
	165−205		8.0 ± 0.7
	205−240		8.0 ± 0.7
	240−300		7.6 ± 0.7

FIG. 11. t spectra as a function of $\cos\theta_{GJ}$ for $M < 1.35$ GeV/c^2.
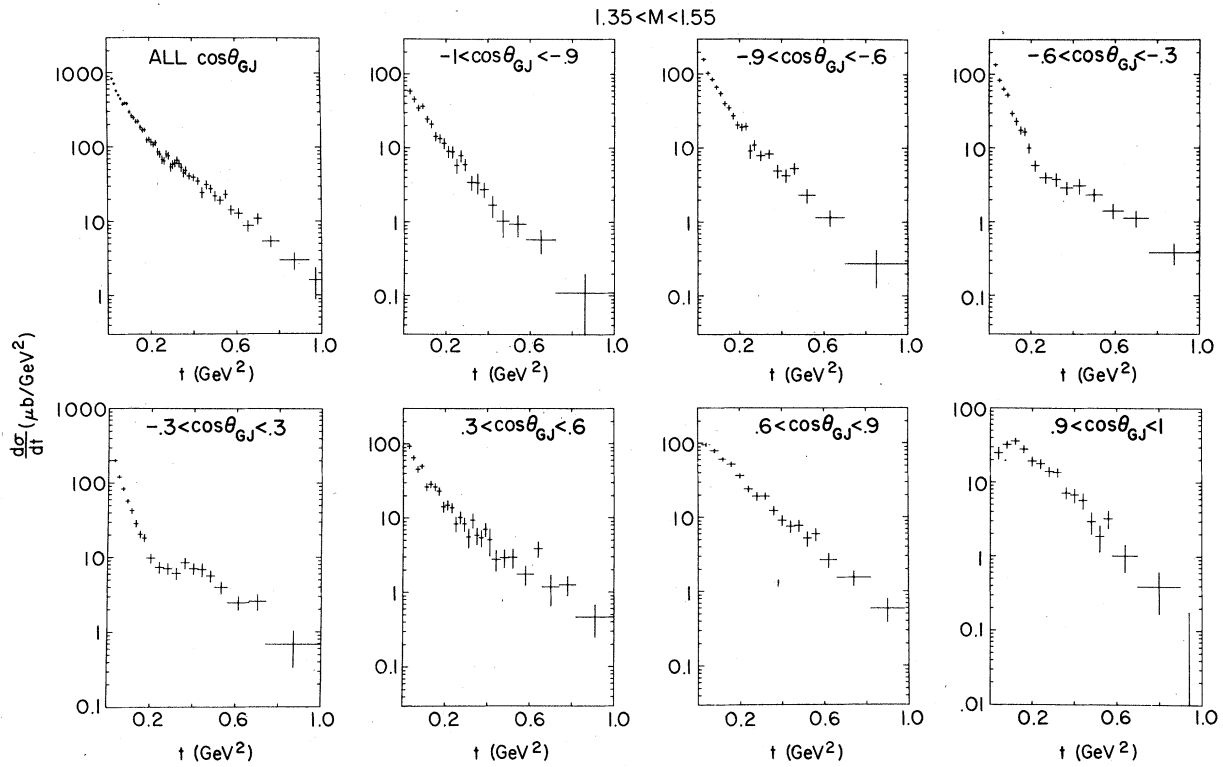
FIG. 12. t spectra as a function of $\cos\theta_{GJ}$ for $1.35 < M < 1.55$ GeV/c^2.
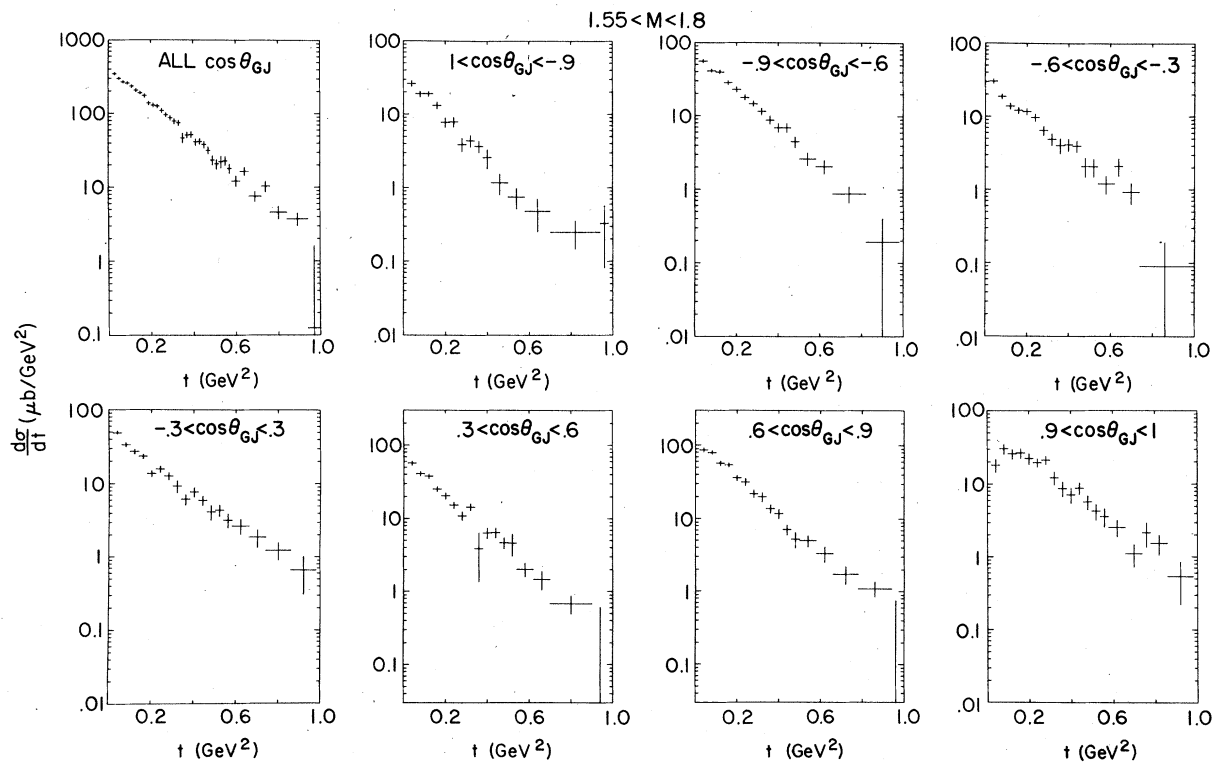
FIG. 13. t spectra as a function of $\cos\theta_{GJ}$ for $1.55 < M < 1.8$ GeV/c^2.

J. BIEL *et al.*
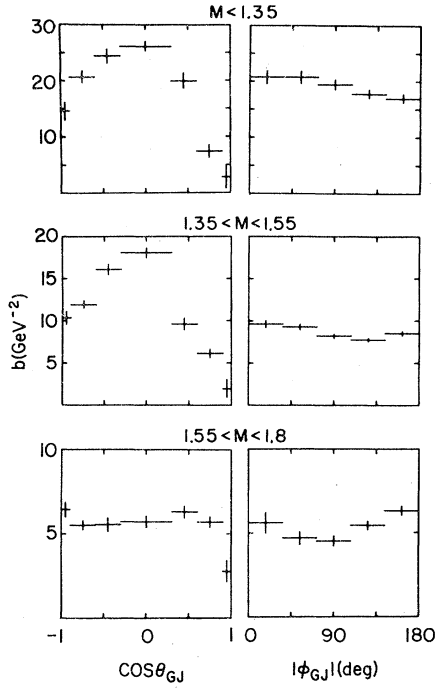
FIG. 14. Slope parameters of t distributions as a function of $\cos\theta_{GJ}$ and $|\phi_{GJ}|$ for three mass regions.

nearly linear, the rate of decrease in b appears smaller between 1.25 and 1.4 GeV. The slope parameter seems to be constant, ~5 GeV^{-2}, for masses greater than 1.6 GeV. [As mentioned previously, corrections were made to total cross sections to account for events with values of t too

small to be detected in our apparatus (t values below 0.02 GeV^2). These corrections were obtained by extrapolating the results given in Table II to $t = 0$.]

2. Momentum dependence

The momentum dependence of the t distribution was investigated using the exponential parametrization described in the previous section. The lower-momentum cutoff $[P_c(M)]$, described in Sec. IV, could not be used in this study; consequently, the investigation was limited to low masses, where biases were minimal. Table III summarizes the results. The data for all mass intervals, with the possible exception of the very lowest one, show only a small increase in b over our beam-momentum range. The weak momentum dependence observed here serves to justify the presentation of our other results in terms of averages over incident momenta.

3. Decay-angle dependence

When data were examined to determine the variations of $d\sigma/dt$ with decay angles of the $(p\pi^-)$ system, a striking effect was observed. The t distribution was found to be insensitive to cuts in ϕ_{GJ},
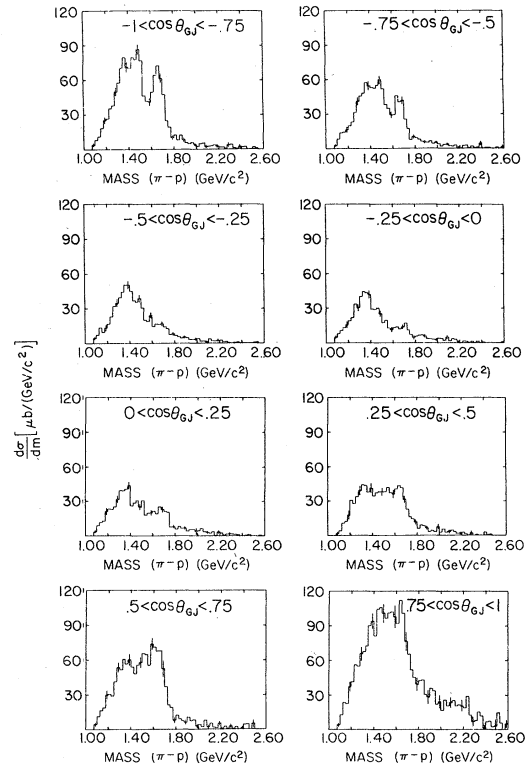

FIG. 15. Mass histograms for six regions of t.

FIG. 16. Mass histograms for six regions of $\cos\theta_{GJ}$.
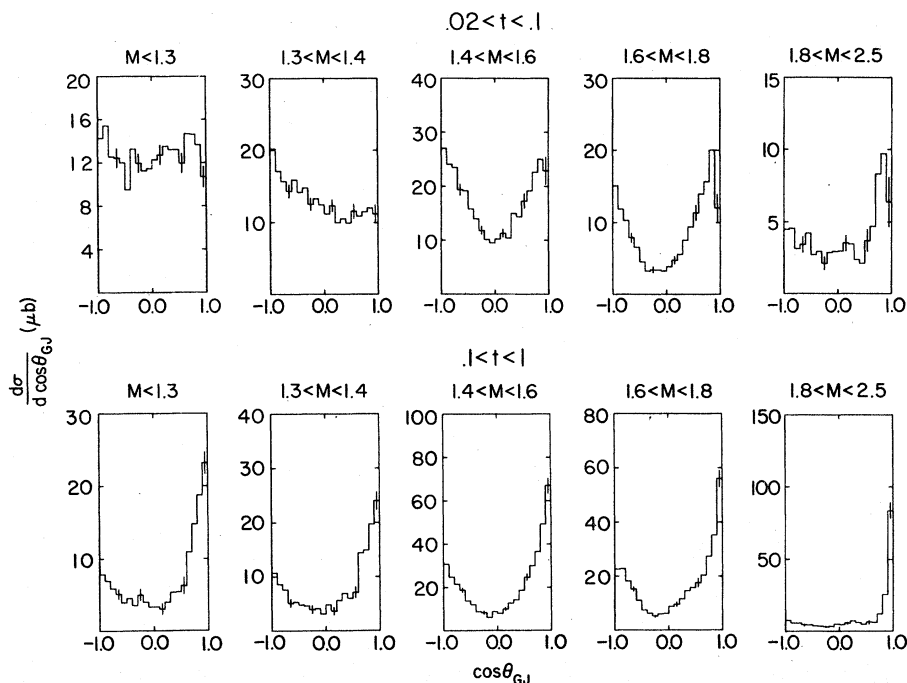
FIG. 17. Distributions in $\cos\theta_{GJ}$ for two regions of t and for five regions of mass.

but was a strong function of θ_{GJ}. As can be seen in Figs. 11–13, the break in $d\sigma/dt$ which occurs at smaller masses is greatly enhanced for central values of $\cos\theta_{GJ}$; data for very large absolute val-ues of $\cos\theta$ show no break at all. For larger mass values, where the overall t distribution is approxi-mately exponential, there is much less variation with $\cos\theta$. All mass intervals suggest the pres-
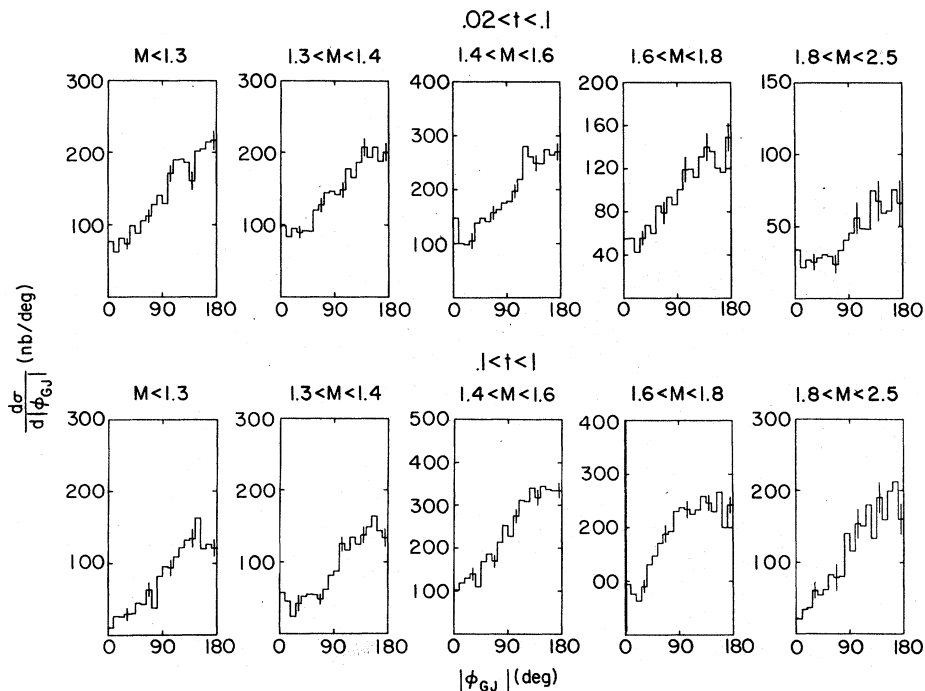
FIG. 18. Distribution in ϕ_{GJ} for two regions of t and five regions of mass.
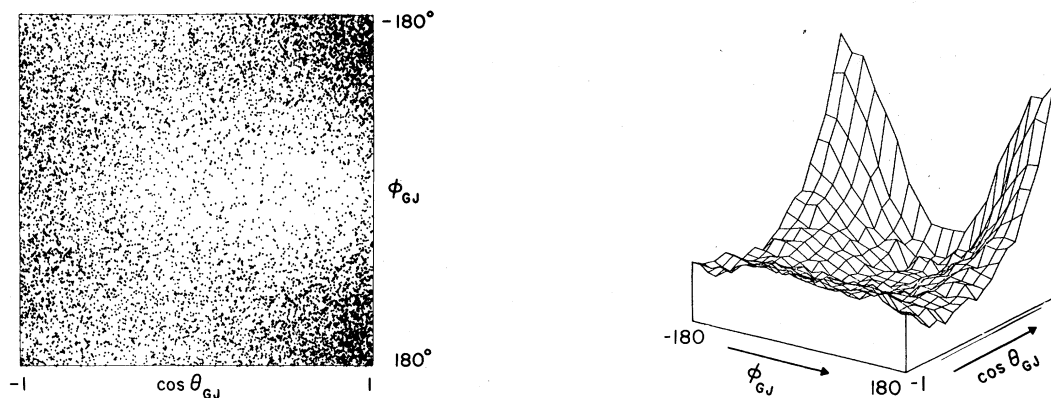
FIG. 19. The cross section as a function of $\cos\theta_{GJ}$ and $|\phi_{GJ}|$ illustrated in both a scatterplot and a perspective drawing.

ence of a turnover in $d\sigma/dt$ near $t = 0$ for large values of $\cos\theta$. This effect can be understood in terms of specific models for diffraction production.[5,8]

Figure 14 shows, for the same three mass intervals studied in Figs. 11–13, the dependence of the slope parameter on $\cos\theta_{GJ}$ and on $|\phi_{GJ}|$. This plot confirms the weak dependence of $d\sigma/dt$ on $|\phi_{GJ}|$, and provides a quantitative measure of the dramatically different values for slopes found for different regions of $\cos\theta_{GJ}$. The small changes of b with $|\phi_{GJ}|$ can be attributed to the known correlation in our data between $\cos\theta_{GJ}$ and ϕ_{GJ}, which will be discussed later.
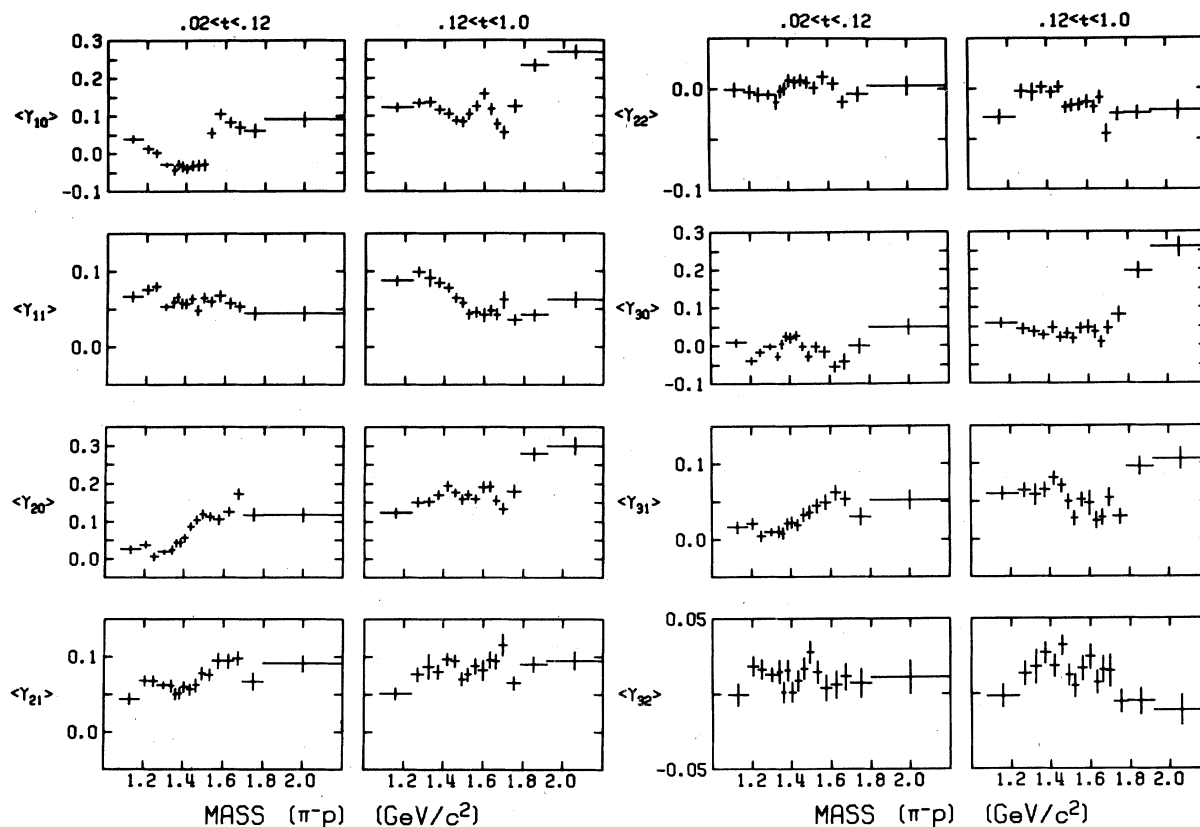
FIG. 20. $\langle \mathrm{Re}(Y_{lm})\rangle$ as a function of mass and t in the Gottfried–Jackson frame.

C. Mass distributions

1. Dependence on t

The strong variation of $d\sigma/dt$ with mass is likewise reflected in the dependence of $d\sigma/dM$ upon t. Figure 15 displays the M distributions for six t regions. At low t, the spectrum is dominated by a low-mass peak at approximately 1.4 GeV. As t is increased, the mean mass value of M also increases, and there appears some evidence for peaks at about 1.5 and 1.7 GeV.

2. Decay-angle distributions

As was the case with the t distributions, the mass spectra show interesting variations as a function of decay angles. Figure 16 illustrates the dependence of $d\sigma/dM$ on $\cos\theta_{GJ}$. For large negative values of $\cos\theta$, there is a striking peak at 1.7 GeV, which seems to be the clearest evidence we have for the production of possible ($p\pi^-$) resonant states. As $\cos\theta$ is increased, the production of this state at first diminishes rapidly and then, at larger positive $\cos\theta$, the peak reappears again, although not as clearly as for $\cos\theta < 0$. It is also evident from this figure that there is a large increase in the cross section at very large

positive $\cos\theta$ for events with masses above 1.8 GeV.

D. Decay-angle distributions

Cross sections, as a function of $\cos\theta_{GJ}$ and $|\phi_{GJ}|$, for all momenta, are given in Figs. 17 and 18 for two t intervals and five mass regions. Our $d\sigma/d|\phi_{GJ}|$ spectra are nearly independent of mass and t, with a common minimum at $|\phi| = 0°$ and a maximum at $|\phi| = 180°$. The dependence of the $\cos\theta_{GJ}$ distribution on mass and t is more pronounced. At small mass and t, $d\sigma/d\cos\theta_{GJ}$ is nearly flat. As the mass is increased, the small-t data show: first, a slight peak at $\cos\theta = -1$, then, nearly equal peaks at the two extremes of $\cos\theta$ and finally, at the highest masses, a single peak near $\cos\theta = 1$. All mass intervals for the high-t data exhibit similar behavior in $\cos\theta$: there is a large peak at $\cos\theta = 1$ and a smaller peak at $\cos\theta = -1$. The data at high t and highest mass have a particularly pronounced peak at $\cos\theta = 1$.

A more dramatic display of the variation of the cross section with the decay angles is given in Fig. 19. This illustration combines a weighted scattergram (left) with a perspective view of a three-dimensional representation of the cross sec-
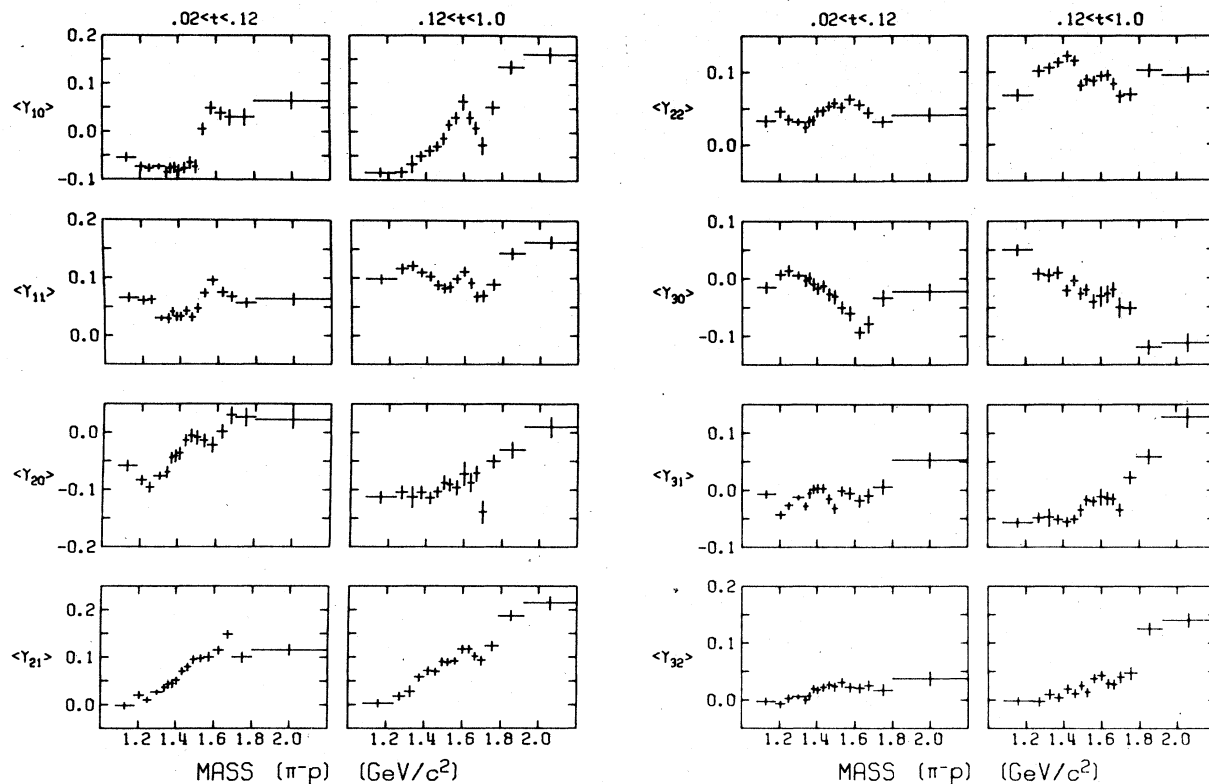

FIG. 21. $\langle \text{Re}(Y_{lm}) \rangle$ as a function of mass and t in the s-channel frame.
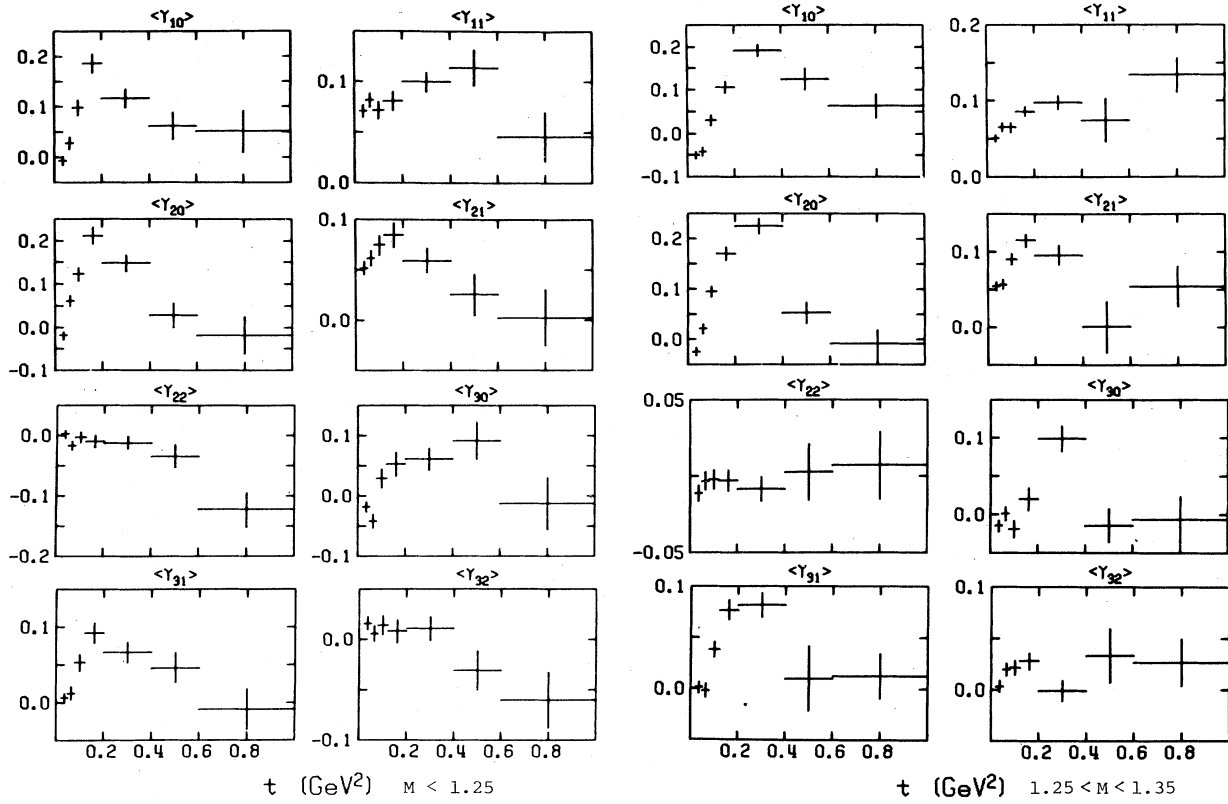
FIG. 22. $\langle \mathrm{Re}(Y_{lm}) \rangle$ as a function of mass and t in the Gottfried-Jackson frame.
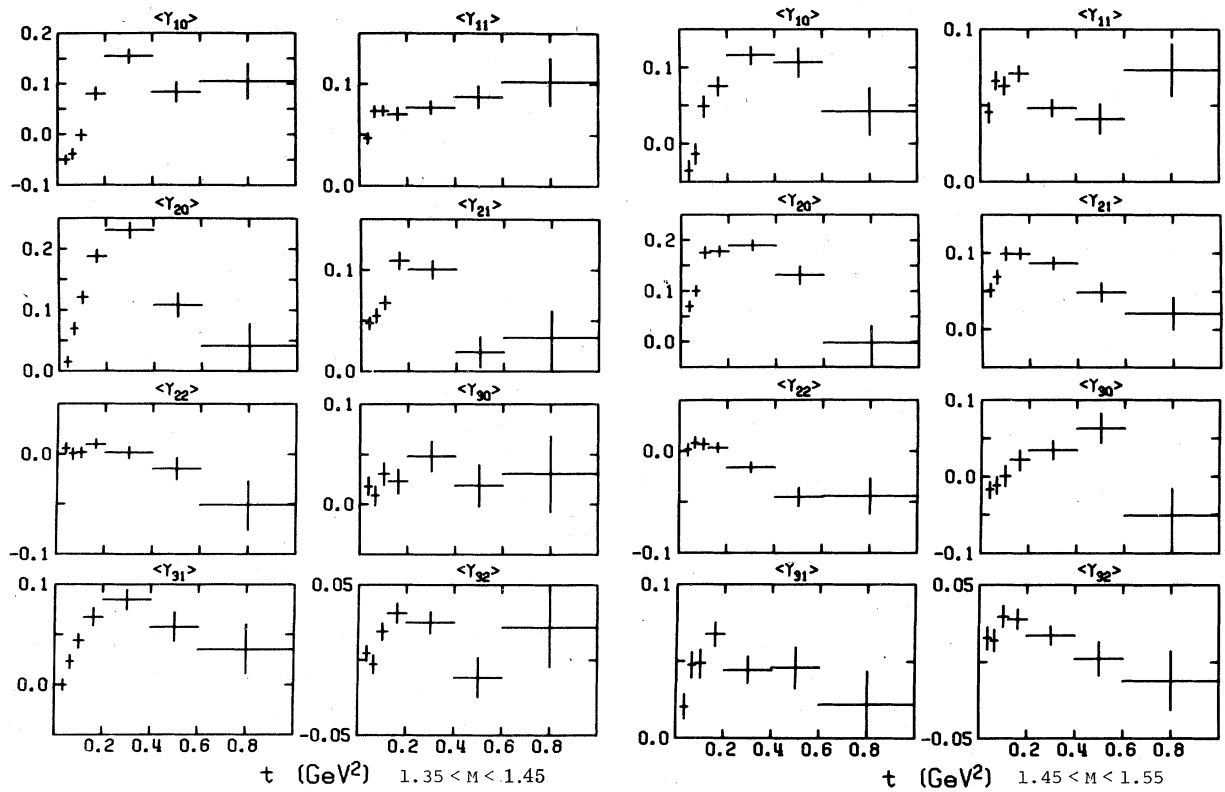

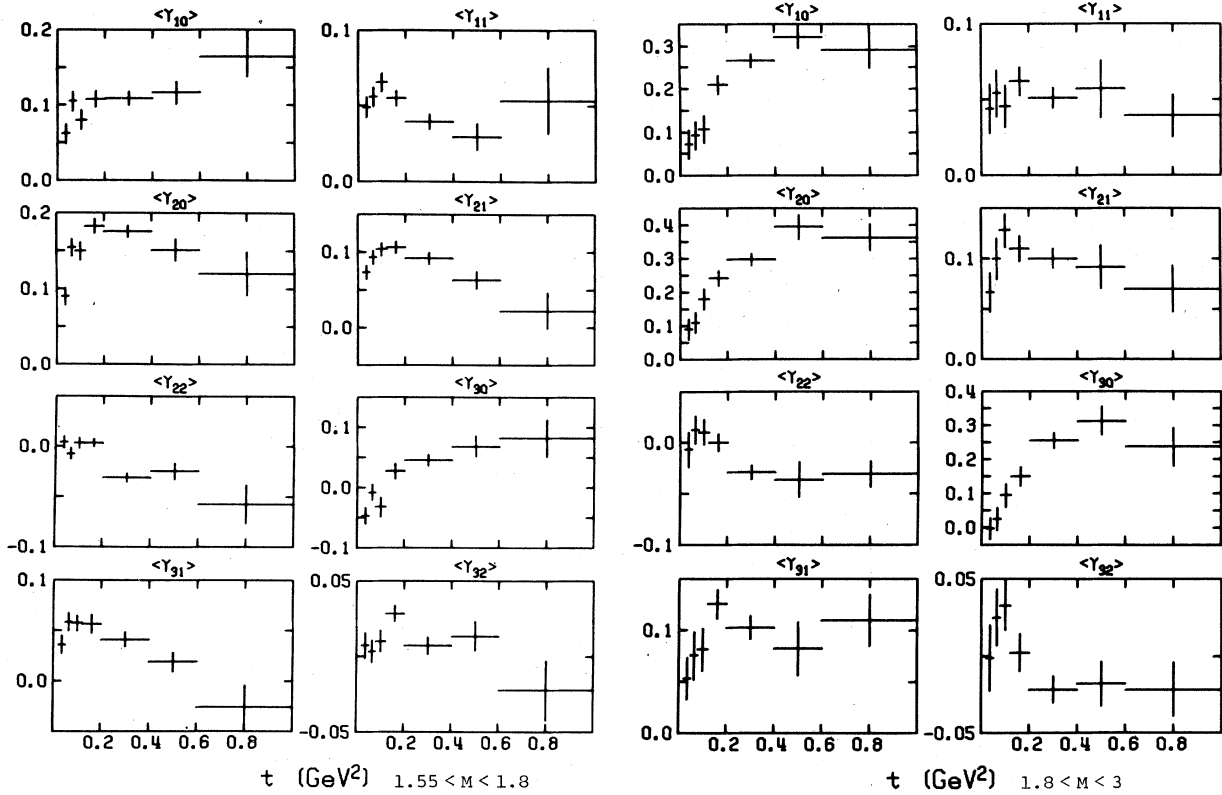FIG. 23. $\langle \mathrm{Re}(Y_{lm}) \rangle$ as a function of mass and t in the Gottfried-Jackson frame.

FIG. 24. $\langle \mathrm{Re}(Y_{lm}) \rangle$ as a function of mass and t in the Gottfried-Jackson frame.
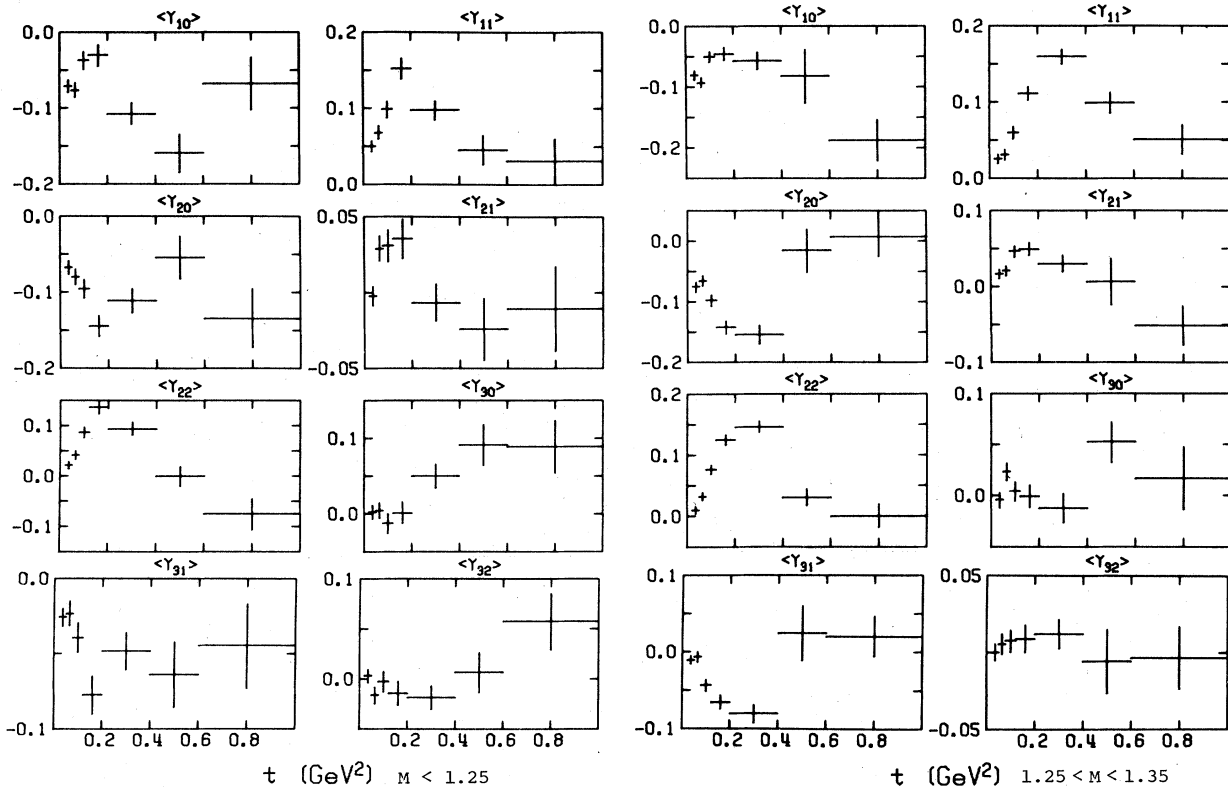
FIG. 25. $\langle \mathrm{Re}(Y_{lm}) \rangle$ as a function of mass and t in the s-channel frame.

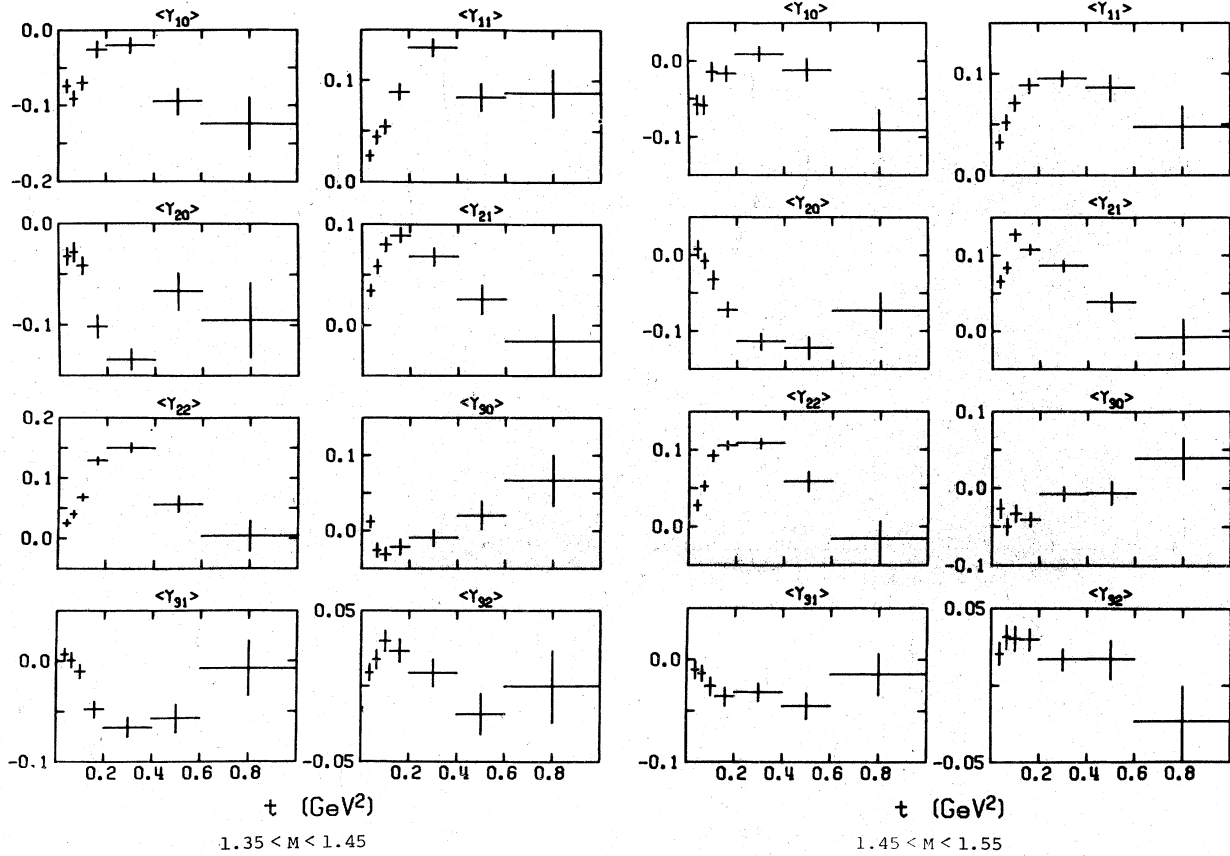1.35 < M < 1.45   1.45 < M < 1.55

FIG. 26. $\langle \text{Re}(Y_{lm}) \rangle$ as a function of mass and t in the s-channel frame.

tion for all data of reaction (1). It is clear that the cross section is largest at large $\cos\theta_{GJ}$ and large $|\phi_{GJ}|$, and varies slowly for negative values of $\cos\theta_{GJ}$.

We have performed a more detailed analysis of the decay angular distributions by decomposing the data into a sum over spherical harmonics. The normalized moments of the spherical harmonics, or simply the "moments", are defined as follows:

$$\langle Y_{lm} \rangle \equiv \frac{\sum_i W_i Y_{lm}(\cos\theta_i, \phi_i)}{\sum W_i}, \qquad (11)$$

where the summation runs over all events, W_i is the total weight for an event, and the angles θ_i and ϕ_i are the decay angles in some particular rest frame of the $(p\pi^-)$ system. For our data, moments were calculated using two sets of mass and two sets of t intervals. In the first calculation, the data were divided into two regions of t, with 17 mass intervals at low t and 16 mass intervals at high t. This gave a detailed mass dependence which is particularly useful in determining what, if any, resonant states are present in the data. A second calculation was performed for seven sepa-

rate t intervals, each divided into six mass intervals. This enabled us to examine in more detail the t dependence of the moments.

Moments were calculated in the helicity and in the Gottfried-Jackson frames for orbital-wave values up to $l = 6$. Both the real and imaginary parts of the moments were calculated, but as mentioned previously, parity conservation requires our data to be symmetric about $\phi = 0$, which implies that the imaginary parts of all moments much vanish. (The results for the imaginary parts of the moments were consistent with this requirement; see Ref. 7 for more detail.) The real parts of the moments up to $l = 3$ and $m = 2$ are plotted in Figs. 20-27. The moments as calculated in the helicity frame are far more complicated than those calculated in the Gottfried-Jackson frame. This is a natural consequence of the dominance of the Deck mechanism[5,8] in the production process. In particular, moments for $m > 2$ are significant in the helicity frame but not so when calculated using the Gottfried-Jackson angles. This is consistent with approximate helicity conservation in the t channel. A complete listing of the values of the
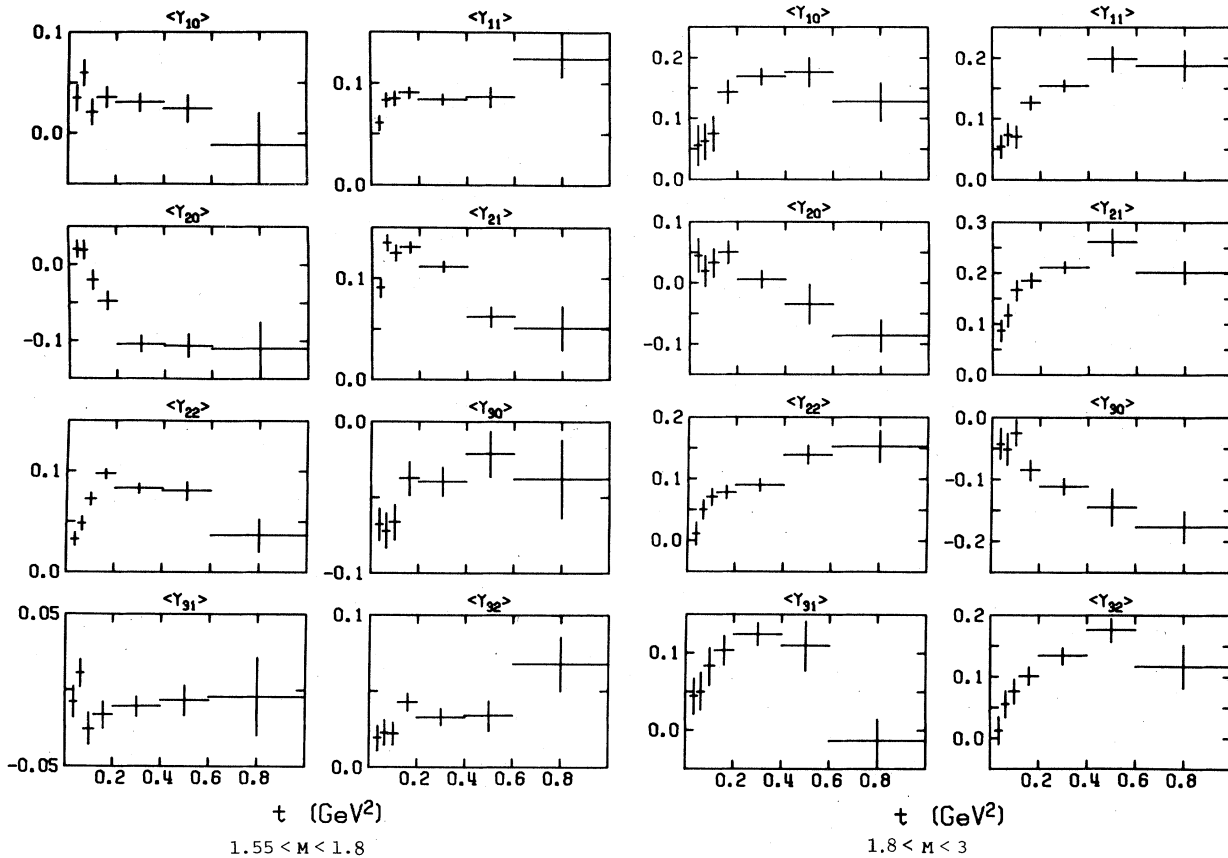
FIG. 27. $\langle \mathrm{Re}(Y_{lm}) \rangle$ as a function of mass and t in the s-channel frame.

moments in the Gottfried-Jackson frame, for quantum numbers up to $l = 6$ and $m = 6$, is available in the Appendix to the preprint of this work.[9]

VI. SUMMARY

Although there is at present no fundamental understanding of the dissociation process, we can nevertheless draw a number of important conclusions from our work. The dissociation cross section which had been falling steadily with increasing momentum at momenta below 50 GeV/c has no significant momentum dependence over our range of incident momenta.[7] In addition to our confirming the strong mass-t correlation characterizing our reaction, we have found a surprising dependence of the t distribution on the polar angle in the

Gottfried-Jackson frame. A complicated mass spectrum, containing apparently both resonant states and a continuum component was observed. Moments of the decay-angle distributions have revealed a rich structure, suggesting contributions from many partial waves. Finally, a measure of success was achieved in explaining the data in terms of a Deck-type model.[5,8] Although a model capable of explaining the details has yet to be worked out, it appears that we are beginning to understand the process of inelastic diffraction.

385 (1976).

[2] M. L. Good and W. D. Walker, Phys. Rev. 120, 1857 (1960).

[3] See, for example, the review of H. Bøggild and T. Ferbel, Annu. Rev. Nucl. Sci. 24, 451 (1974).

[4] See, for example, D. Leith, in *The Strong Interactions*, SLAC Summer Institute on Particle Physics, 1974 edited by M. Zipf (National Technical Information Service, U.S. Dept. of Commerce, Springfield, Va., 1974).

[5] J. Biel *et al*., Phys. Rev. Lett. 36, 504 (1976); J. Biel *et al*., *ibid*. 36, 507 (1976); J. Biel *et al*., Phys. Lett.

65B, 291 (1976).

[6] M. Longo *et al*., University of Michigan Report No. UM-HE 74-18 (unpublished).

[7] For more details see J. Biel, Ph.D. thesis, University of Rochester Report No. UR-614, 1977 (unpublished).

[8] See, for example, R. Cutler and E. Berger, Phys. Rev. D 15, 1903 (1977); I. A. Ponomarev, Report No. ITEP-96, Moscow 1977 (unpublished).

[9] J. Biel *et al*., University of Rochester Report No. UR-656 (unpublished).